Bioinspiration &
Biomimetics

PURPOSE-LED
PUBLISHING™

PAPER

A biomimetic underwater vehicle actuated by waves with ionic polymer–metal composite soft sensors

To cite this article: Qi Shen *et al* 2015 *Bioinspir. Biomim.* **10** 055007

View the article online for updates and enhancements.

You may also like

- Kirigami-inspired self-powered pressure sensor based on shape fixation treatment in IPMC material
Jen-Hahn Low, Pei-Song Chee, Eng-Hock Lim et al.
- Distributed flow estimation and closed-loop control of an underwater vehicle with a multi-modal artificial lateral line
Levi DeVries, Francis D Lagor, Hong Lei et al.
- Influence of environmental conditions and voltage application on the electromechanical performance of Nafion-Pt IPMC actuators
Allison M Arnold, Ji Su and Edward M Sabolsky

GAS

BreathSpec®

The combination of GC and IMS enables a physical separation to detect volatiles without pre-concentration directly sampled from human breath.

Our GC-IMS based analyzer allows instant breath sampling and analysis of volatiles in minutes.

The transportable GC-IMS facilitates versatile sampling incl. direct exhalation, syringe based and also gas bags for sampling of breath and static body headspace (oral/nasal/skin).

▶▶▶ click for more details

This content was downloaded from IP address 131.216.14.8 on 07/04/2026 at 18:17

Bioinspiration & Biomimetics

PAPER

A biomimetic underwater vehicle actuated by waves with ionic polymer–metal composite soft sensors

Qi Shen[1,2], Tianmiao Wang[1] and Kwang J Kim[2]

[1] Robotic Institute, School of Mechanical Engineering and Automation, Beihang University, Beijing 100191, People's Republic of China
[2] Mechanical Engineering Department, University of Nevada—Las Vegas, Las Vegas, NV 89154-4027, USA

E-mail: kwang.kim@unlv.edu

RECEIVED
14 February 2015

REVISED
26 May 2015

ACCEPTED FOR PUBLICATION
7 July 2015

PUBLISHED
28 September 2015

Keywords: ionic polymer–metal composite, soft sensor, biomimetic underwater vehicle

Abstract

The ionic polymer–metal composite (IPMC) is a soft material based actuator and sensor and has a promising potential in underwater application. This paper describes a hybrid biomimetic underwater vehicle that uses IPMCs as sensors. Propelled by the energy of waves, this underwater vehicle does not need an additional energy source. A physical model based on the hydrodynamics of the vehicle was developed, and simulations were conducted. Using the Poisson–Nernst–Planck system of equations, a physics model for the IPMC sensor was proposed. For this study, experimental apparatus was developed to conduct hydrodynamic experiments for both the underwater vehicle and the IPMC sensors. By comparing the experimental and theoretical results, the speed of the underwater vehicle and the output of the IPMC sensors were well predicted by the theoretical models. A maximum speed of 1.08×10^{-1} m s^{-1} was recorded experimentally at a wave frequency of 1.6 Hz. The peak output voltage of the IPMC sensor was 2.27×10^{-4} V, recorded at 0.8 Hz. It was found that the speed of the underwater vehicle increased as the wave frequency increased and the IPMC output decreased as the wave frequency increased. Further, the energy harvesting capabilities of the underwater vehicle hosting the IPMCs were tested. A maximum power of 9.50×10^{-10} W was recorded at 1.6 Hz.

1. Introduction

Autonomous underwater vehicles have been widely studied and used all over the world during the past decades [1–11]. A challenge in underwater operations is for underwater vehicles to become more energy efficient, and thus have greater endurance during missions. Moreover, the need for clean power has been increasing.

The applications of smart materials have significantly contributed to the development of underwater vehicles [12–14]. The ionic polymer–mental composite (IPMC), one type of electroactive polymer, has the potential as a soft underwater sensor [15]. An IPMC is composed of a polymer membrane that has separated electrodes chemically affixed to both sides [16–18]. The most interesting characteristic of the IPMC is its inherent softness. If the IPMC is under an electric field, the ions will begin to redistribute, and the IPMC will bend accordingly. As a result, biomimetic underwater robots that are IPMC-actuated have been widely studied [19–25]. If a mechanical stimulus is applied, the mobile ions will distribute in the polymer, and a detectable voltage will be generated. As a result, the IPMC can be used as a soft sensor and as an energy-harvesting device, with applications in many fields.

This current study theoretically modeled and experimentally investigated a biomimetic underwater vehicle that uses IPMC as soft sensors.

1.1. Dynamic modeling of the underwater vehicle

Recently, an increasing number of systems powered by clean energy have been developed and used around the oceans of the world. For example, a snakelike wave-power generator has been developed [26] in which the relative motion between its parts converts wave energy into electric power. Similar conceptions have been applied to ships and autonomous vehicles.

Specifically, the Wave Glider®, developed by Liquid Robotics, Inc., is a wave-propelled autonomous marine vehicle [27] based on biogeochemical energy. It can operate as long as one year. Recently,

© 2015 IOP Publishing Ltd

Manley and Willcox [28] developed an unmanned maritime vehicle whose platform could be propelled utilizing the energy from ocean waves. They used a submerged multiple-wing system that produces the propulsion force, and a cable to connect the submerged system with a surface float device. Solar panels on the float device were used as the power source for the onboard electronics.

To date, few studies have focused on biomimetic underwater vehicles using clean energy or the hydrodynamics of these vehicles. In this current study, a main goal was to develop a soft material embedded biomimetic underwater vehicle. A theoretical model of the vehicle was developed. The model was validated in experiments on the prototype, which was a free-swimming underwater vehicle.

1.2. Underwater sensors using IPMCs

IPMCs have been widely studied for their application in underwater sensors [29–34]. In particular, the sensing and energy-harvesting performance of IPMCs have been extensively studied. Chen *et al* [35] proposed a model for IPMC sensors that could predict the short-circuit sensing currents under applied deformations. Recently, Abdulsadda and Tan proposed a biomimetic artificial lateral-line system, based on the IPMC sensors, for underwater robots and vehicles [36]. Later, they used an estimation approach based on an analytical model was tested with good accuracy by using IPMC flow sensors to localize a moving underwater vibrating sphere [37]. Aureli *et al* [38] demonstrated the energy-harvesting capability of submerged IPMCs under base excitations; they developed a model for energy that was harvested based on the vibration of IPMCs. In addition, two studies analyzed energy scavenging, one evaluating the weaving of an underwater flag [39] and the other the beating of a biomimetic fish tail [40]; both studies hosted IPMC sensors. Tiwari and Kim studied the effects of various IPMC parameters on battery charging in the mechanical and electrical domains [41].

However, little research has been done on underwater vehicles having IPMC sensors. Therefore, another goal of this study was to investigate the sensing capabilities of IPMCs applied to the underwater vehicle to measure the amplitudes and frequencies of the waves. In this current study, IPMC sensors were applied to the underwater vehicle; specifically, they were attached to the soft fins of the vehicle. A model was developed to describe the charge redistribution dynamics in the polymer. Experiments were conducted to validate the model. In addition, the energy-harvesting capabilities of IPMC in current system were tested.

The main difference between the underwater vehicle presented in this paper and the ones proposed previously is the fins that produce thrust. The fins in the current prototype of this study were flexible while the previous vehicles' fins were rigid. In previous studies, it was found that a two-dimensional flexible flapping foil had higher thrust efficiency (up to 36%) than a rigid flapping foil [42].

The reason IPMCs were used in the vehicle for this study to test sensing and energy harvesting is because, compared with other sensors, such as strain gages and magnetic encoders, IPMC has the following advantages. From the point of view of machinery, IPMCs are soft, thus can avoid additional interference to the soft fins. From the point of view of electronics, an IPMC sensor can generate output voltage; thus, no extra power is needed to be applied on the IPMC. Finally, an IPMC sensor can operate in water, and does not need extra waterproofing. Thus, this current study can provide an optimal design for the underwater vehicle as well as a better understanding of IPMC sensors in underwater systems.

2. Materials and methods

2.1. Underwater vehicle

2.1.1. Experimental setup

The manta ray is a fish typical of the type that uses median and/or paired fins for aquatic locomotion. The flapping motions of a manta ray's fins in water mimic the motion of birds' wings; thus, the manta ray can move with high efficiency, maneuverability, and stability [43]. During this study, a biomimetic underwater vehicle was developed that was actuated by waves, inspired by the means of propulsion used by the manta ray. Regarding the design of the underwater vehicle, figure 1 shows the prototype for the wave glider. The vehicle consists of three parts:

(1) the float on the water surface, which provides the buoyancy;

(2) the underwater glider, which produces the thrust;

(3) the cables that connect the float and the glider.

An airtight container (Lock & Lock Co., Ltd, S. Korea) was used as the float. The glider was designed in SolidWorks, and was fabricated with acrylonitrile–butadiene–styrene plastic. To obtain a smooth surface, the glider was covered with black-matte resin varnish. To produce the thrust, four films were used as the soft fins. The fins were attached to the cylindrical beams. Small rectangular copper sheets, which were set inside the cylindrical beams, were used to clamp the IPMC sensors to the fins.

Independent of wave direction, wave energy is converted into forward thrust for the propulsion of the underwater vehicle. The propulsion system of the vehicle used in this study was purely a mechanical structure, so this vehicle did not need to use electrical power. The flapping motion of a manta ray's wing-like fins, producing a forward force, inspired the design.

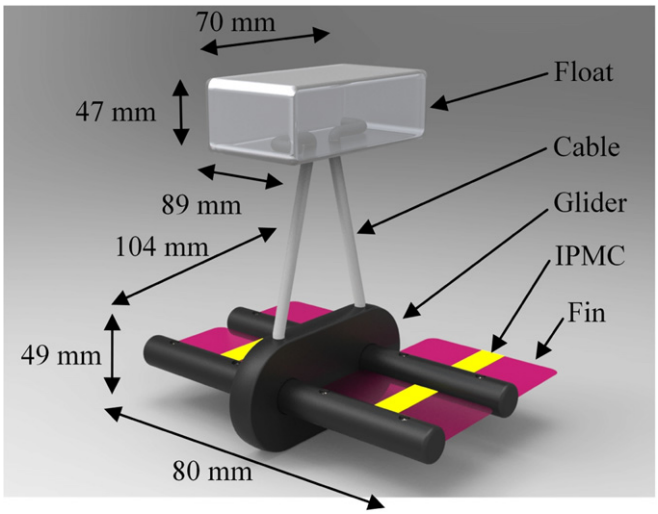

Figure 1. Prototype of the underwater vehicle.

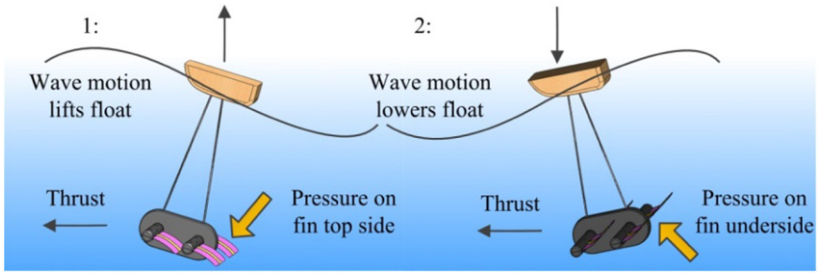

Figure 2. The mechanics of the vehicle's propulsion system.

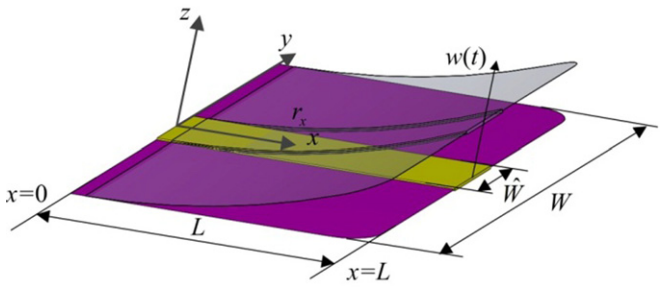

Figure 3. Geometric definitions of the film used as a fin in the vehicle.

The submerged glider had a vertical movement, with the water around the glider being relatively static. A forward propulsion force generated by the wings was converted based on a portion of this up-and-down motion. As ocean waves passed by the wings on the surface, the entire system was pulled by the submerged glider towards a predetermined direction, as shown in figure 2. It was critical for the vehicle design that the glider was split from the float. Without the tail of the glider, the total length of the vehicle was 104 mm. The glider was 49 mm in height and 80 mm in width. The glider weighed approximately 84 g. The length, thickness, and width of the float were 89 mm, 47 mm, 70 mm, respectively. Each film for the wings was 40 mm long, 30 mm wide, and 0.015 mm thick.

2.1.2. Modeling

Regarding the film dynamics in fluid, it was assumed in this study that the film used as the fin of the vehicle satisfied the following constraints:

(1) the nominal thickness of the film is greatly exceeded by its length;

(2) the oscillation of the film, denoted by $w(z, t)$, is far smaller compared to the length.

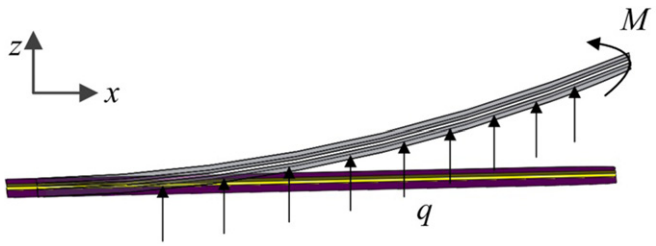

Figure 4. Schematic of the replaced hydrostatic force and moment acting on the film.

The film was assumed to deform periodically at z, as shown in figure 3.

To obtain the dynamic model of the film in water, the governing equation of the film dynamic deflection $w(z, t)$ can be denoted [44] as:

$$YI\frac{\partial^4 w(x,\ t)}{\partial x^4} + \mu\frac{\partial^2 w(x,\ t)}{\partial t^2} = F(x,\ t), \tag{1}$$

where Y, I, μ, F, x, and t are Young's modulus, the moment of inertia of the film, the mass per unit length of the film, the external applied force per unit length acting on the film, the spatial coordinate along the length of the film, and time, respectively. Sader [45] described in detail of the boundary layer for the conditions of (1). Converting (1) into the Laplace domain, the following equation is obtained:

$$\frac{YI}{L^4}\frac{\partial^4 w(x,\ s)}{\partial x^4} + \mu s^2 w(x,\ s) = F(x,\ s), \tag{2}$$

where x has been non-dimensionalized by the length of the film, L, and refers to its scaled quantity. This convention will be applied henceforth.

Assuming that the coordinate on the solid body of the underwater vehicle is static, the soft wings and nearby water are in motion relative to the underwater vehicle. According to D'Alembert's inertial force theory, an inertial force acts on the film. Based on the dynamics of the film in a liquid, the applied forces on the film have two components, the hydrodynamic force, $F_{\text{hydro}}(x,\ s)$, and the inertial force, $F_{\text{drive}}(x,\ s)$:

$$F(x,\ s) = F_{\text{hydro}}(x,\ s) + F_{\text{drive}}(x,\ s). \tag{3}$$

The hydrodynamic force, $F_{\text{hydro}}(x,\ s)$, acting on the film can be expressed as:

$$F_{\text{hydro}}(x,\ s) = -\frac{\pi}{4}\rho_w s^2 W^2 \Gamma_1(\omega) w(x,\ s), \tag{4}$$

where W is the width of the film. $\Gamma_1(\omega)$ is the dimensionless hydrodynamic function of the film [45], and ρ_w is the density of the liquid. By substituting (3) and (4) into (2), and rearranging, the beam dynamics equation becomes:

$$\frac{\partial^4 w(x,\ s)}{\partial x^4} - \frac{\left(-\mu - \frac{\pi}{4}\rho_w W^2 \Gamma_1(\omega)\right)L^4}{YI} s^2 w(x,\ s) = \frac{F_{\text{drive}}(x,\ s)}{YI}L^4. \tag{5}$$

For simplicity, (5) can be rewritten as:

$$\frac{\partial^4 w(x,\ s)}{\partial x^4} - B^4(s)\, w(x,\ s) = C(x,\ s), \tag{6}$$

where:

$$B(s) = \left[\frac{\left(-\mu - \frac{\pi}{4}\rho_w W^2 \Gamma_1(\omega)\right)L^4 s^2}{YI}\right]^{1/4} C(s) = \frac{F_{\text{drive}}(x,\ s)}{YI}L^4.$$

To obtain the analytic solution of (6), the theory of Green's functions is used. Sader [45] used the expression $G(x, x', s)$, where x' is the variable in Green's function related with x. At this point, the general solution for (6) becomes:

$$w(x,\ s) = \int_0^1 G(x,\ x',\ s)\, C(x',\ s)\, \mathrm{d}x', \tag{7}$$

where (7) is the deflection function of film oscillating in a viscous fluid.

The inertial force acting on the film is replaced by two components, a distributed force density, q, acting along the length, and a moment, M, acting at the film tip. The distributed force density, q, can be given as:

$$qL = m\frac{\partial^2 D_w(t)}{\partial t^2}, \tag{8}$$

where m represents the mass of the film and $D_w(t)$ is the wave motion on the surface. The Laplace transform of (8) is converted to obtain:

$$q(\mathrm{s}) = \frac{mD_w(s)s^2}{L}. \tag{9}$$

The moment acting on the film is:

$$M(s) = \int_0^L q(\mathrm{s})x\mathrm{d}x = \frac{mD_w(s)Ls^2}{2}. \tag{10}$$

The distributed force density and the moment can be seen in figure 4.

The deflection of the film, as be described by Sader [45], is:

$$w(x, s) = \frac{L^4}{YI}\left(\int_0^1 G(x, x', s) q(s) x' \mathrm{d}x' + M(s) \left.\frac{\partial G(x, x', s)}{\partial x'}\right|_{x'=1}\right). \quad (11)$$

By substituting (9) and (10) into (11), the transfer functions can be obtained, $R(x, s) = w(x, s)/D_w(s)$ and $R_d(x, s) = \partial w(x, s)/\partial z/D_w(s)$. Given the surface-wave motion, $D_w(t) = A_D \sin(\omega t)$, to the underwater vehicle, the oscillation displacement and the slope of the film at the tip, $z = L$, can be denoted as:

$$w(L, t) = A_D \left|R(L, j\omega)\right| \sin(\omega t + \angle R(L, j\omega)), \quad (12)$$

$$\left.\frac{\partial w(L, s)}{\partial z}\right|_{z=L} = A_D \left|R_d(L, j\omega)\right| \sin\left(\omega t + \angle R_d(L, j\omega)\right), \quad (13)$$

where $\angle(\cdot)$ denotes the phase angle.

Assuming the resulting force caused by the water acting on the float is zero in the horizontal direction, the system is propelled by the force produced by the film. At steady state, the vehicle achieves a periodic, forward motion with the speed. The hydrodynamic force acting on each point x of the film can be denoted as:

$$F_x(x, t) = -\rho_w \frac{\pi}{4} W^2 \Gamma_x(\omega) a_{x\perp}(x, t), \quad (14)$$

where $\Gamma_x(\omega)$ is the hydrodynamic function for the film subject to an oscillation with radial frequency ω and $a_{x\perp}$ is the acceleration virtual to point x, expressed as:

$$\begin{aligned} a_{x\perp}(x, t) &= a_x(x, t) \cos\theta(x, t), \\ &= \frac{\mathrm{d}U(x, t)}{\mathrm{d}t} \cos\theta(x, t), \\ &= \frac{\mathrm{d}^2 w(x, t)}{\mathrm{d}t^2} \cos\theta(x, t), \end{aligned} \quad (15)$$

where $U(x, t)$ is the speed on point x. Since the displacement of the film at z is small compared to its length, the slope $\tan\theta(x, t)$ on point x approximates the angle $\theta(x, t)$. This is expressed as:

$$\theta(x, t) \approx \tan\theta(x, t) = \frac{\partial w(x, t)}{\partial z}. \quad (16)$$

Then, the thrust force produced by a single film can be denoted as:

$$T(t) = \int_0^1 F_x(x, t)\mathrm{d}x = \frac{\pi}{4}\rho_w W^2 \Gamma_x(\omega)\omega^2 A_D \times \int_0^1 \left(\begin{array}{l} \left|R(x, j\omega)\right| \sin(\omega t + \angle R(x, j\omega)) \\ \times \cos\left(A_D \left|R_d(x, j\omega)\right| \sin \right. \\ \left. \quad \times \left(\omega t + \angle R_d(x, j\omega)\right)\right) \end{array} \right) \mathrm{d}x. \quad (17)$$

The cruising vehicle experiences a drag force, F_D:

$$F_D(t) = \frac{C_D \cdot \rho_w \cdot U(t)^2 \cdot S}{2}, \quad (18)$$

where C_D is the drag coefficient, $U(t)$ is the swimming speed of the underwater vehicle in the forward direction, and S is the wetted surface area. The force balance is explained by:

$$4T(t) - F_D = m\dot{U}(t). \quad (19)$$

Based on (17), (18), and (19), $U(t)$ can be obtained.

2.1.3. Experimental investigation

The drag coefficient relates to the glider body, especially the Reynolds number; the properties of the glider's surface; and the fitness ratio of the body. The slender body theory was utilized in this study to identify the drag coefficient, using a method that was presented in [20–24]. A horizontal servo towing system was used to identify the drag coefficient, C_D. The underwater vehicle was towed under the system, which had a force detection apparatus attached to it, as shown in figure 5. The force transducers measured the forces T_1 and T_2.

The lever principle was used to amplify the resultant force on the vehicle. The force sensors measured the external force T_{ext} acting on the vehicle by $T_{\mathrm{ext}} = (T_1 - T_2)/100$. The experimental results were recorded by a data recorder (Nicolet Vision XP, LDS Inc., Germany). The towing speeds of the underwater vehicle varied from 0.005 to 0.1 m s^{-1}.

In order to validate the speed model, the wave generator—the prototype of which is shown in figure 6—was used to test the underwater vehicle in a tank. The wave generator was designed using a crank-slider mechanism. A DC motor (36SYK71, Saegmotor Co., China) provided the motion for the mechanism. A beam was fixed vertically at the end of the slider to generate the waves. Two other sliders, which were fixed vertically at the two ends of the beam, slid on two fixed rails. The amplitude and frequency of the translational motion could be adjusted by changing the length of the crank and the rotation speed of the motor. The motor was monitored by a motor controller (BDMC4810, Beijing UPTECH Robotics Co. Ltd, China). A computer was utilized to control the motor controller. The waves were generated by the apparatus to mimic the sinusoid up-and-down motion of ocean waves.

The underwater vehicle was propelled by the waves in the tank; at steady state, the vehicle moved through the given range of 10 cm. A timer was used to record the time. The amplitude of the sinusoidal wave was adjusted to 10 mm. The frequencies of the waves varied from 0.4 to 1.6 Hz, which were within the normal frequency range of the ocean waves [46]. Figure 7 shows a snapshot of the vehicle swimming in the tank. The vehicle swimming time was tested three times

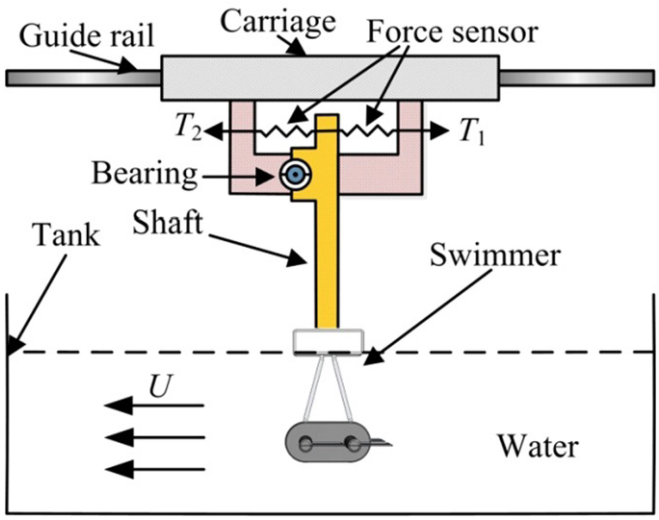

Figure 5. The system used to measure the drag of the glider.

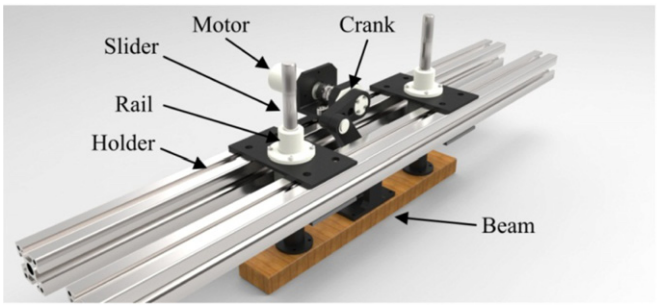

Figure 6. The prototype of the wave generator.

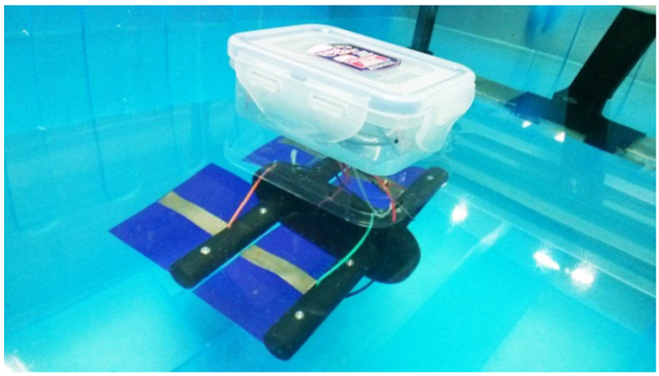

Figure 7. The underwater vehicle tested in a tank to validate the speed model.

under each wave frequency. The cruising speed, U_{exp}, was obtained by the average.

2.2. IPMC underwater sensor

2.2.1. Modeling

The model for the IPMC sensors will be derived in this section. The variables L, $\hat{W}$, and $2h$ represent the length, width, and thickness, respectively, of the IPMC sensor. The Nernst–Planck equation describes the ionic migration and diffusion throughout the polymer as:

$$\frac{\partial C}{\partial t} + \nabla \cdot \left(-D \nabla C - \hat{z} \hat{\mu} \hat{F} \hat{C} \nabla \phi \right) = 0, \qquad (20)$$

where C, D, $\hat{\mu}$, $\hat{F}$, $\hat{z}$, and ϕ are the cation concentration, the diffusion constant, the mobility of cations,

the Faraday constant with a value of $\hat{F} = 96487\ \mathrm{C\ mol^{-1}}$, the charge number, and the electric potential in the polymer, respectively.

The anions are fixed in the polymer matrix. With mobile cations within the polymer, the concentration and migration of ions vary in the deformed IPMC. Thus, the electric field increases at the polymer boundary. This is described with Poisson's equation:

$$\nabla \cdot E = -\nabla^2 \phi = \frac{\rho_c}{\hat{\varepsilon}}, \tag{21}$$

$$\rho_c = \hat{F}\left(\hat{C} - C_0\right), \tag{22}$$

where E, $\hat{\varepsilon}$, ρ_c, C_0 are the strength of the electric field, the absolute dielectric constant, the charge density, and the constant anion concentration, respectively. Since $\hat{\varepsilon}\nabla E \ll \hat{F}C_0$ [35], by combining (20), (21), and (22), one can obtain:

$$\frac{\partial \rho_c}{\partial t} - D\frac{\partial^2 \rho_c}{\partial z^2} + \frac{\hat{z}\hat{\mu}\hat{F}^2 C_0}{\hat{\varepsilon}}\rho_c = 0. \tag{23}$$

Transferring (23) from the time domain to the Laplace domain, (23) can be rewritten as:

$$\rho_c(z, x, s)s - D\frac{\partial^2 \rho_c(z, x, s)}{\partial z^2} + \frac{\hat{z}\hat{\mu}\hat{F}^2 C_0}{\hat{\varepsilon}}\rho_c(z, x, s) = 0. \tag{24}$$

Based on Nemat–Nasser and Li's theory [47], the induced stress is assumed to be proportional to the charge density at the boundary of $z = \pm h$:

$$\sigma(\pm h, x, s) = \alpha \rho_c(\pm h, x, s). \tag{25}$$

where α is the coupling constant. Considering the boundary condition, $\rho_c(h, x, s) + \rho_c(-h, x, s) = 0$, and by solving (24), one obtains:

$$\rho_c(z, x, s) = 2\hat{C}(s)(L - x)\sinh\left(\hat{A}(s)z\right), \tag{26}$$

where:

$$\hat{A}(s) = \sqrt{\frac{\hat{B} + s}{D}}\ \hat{B} = \frac{z\hat{\mu}\hat{F}^2 C_0}{\hat{\varepsilon}}.$$

By relating $\sigma(\pm h, x, s)$ to external stimuli, the expression of $\hat{C}(s)$ is denoted as [35]:

$$\hat{C}(s) = \frac{3Y_{\mathrm{IPMC}}h\hat{A}(s)}{4\alpha L^3 \hat{W}\left(\hat{A}(s)h\cosh(A(s)h) - \sinh\left(\hat{A}(s)h\right)\right)} \times w(s), \tag{27}$$

where Y_{IPMC} is the Young's modulus and $Y_{\mathrm{IPMC}} = 90.92$ MPa. The ionic flux in the z direction is denoted as:

$$f(z, x, s) = -D\left[\frac{1}{\hat{F}}\frac{\partial \rho_c(z, x, s)}{\partial z} - \frac{\hat{F}C_0}{\hat{R}T_a}E(z, x, s)\right], \tag{28}$$

where $\hat{R}$ represents the gas constant and equals $8.3143\ \mathrm{J\ mol^{-1}\ K^{-1}}$ and T_a represents the absolute temperature and equals 297 K. Based on the boundary condition, $f(h, x, s) = f(-h, x, s) = 0$ and $E(\pm h, x, s) \neq 0$, by using (21), (26), and (27), the electric potential of the IPMC can be expressed as:

$$\phi(z, x, s) = -2\hat{C}(s)(L - x)\frac{\sinh\left(\hat{A}(s)z\right)}{\hat{\varepsilon}\hat{A}(s)} + 2\hat{C}(s)(L - x)\cosh\left(\hat{A}(s)h\right) \times \left(\frac{RT_a\hat{A}(s)}{\hat{F}^2 C_0} - \frac{1}{\hat{\varepsilon}\hat{A}(s)}\right)z + b(x, s). \tag{29}$$

The surface electric potential of the IPMC at an open circuit is $\phi(\pm h, 0, s) = \pm V(s)/2$. The output voltage of IPMC at an open circuit is:

$$V(s) = \phi(h, 0, s) - \phi(-h, 0, s) = -4\hat{C}(s)L\frac{\sinh\left(\hat{A}(s)h\right)}{\hat{\varepsilon}\hat{A}(s)}. \tag{30}$$

The transfer function relating the output voltage to the tip displacement, $H(s) = V(s)/w(s)$, can be obtained. Given the tip displacement of the soft films in (12), and converting (30) into the time domain, the output voltage of the IPMC can be denoted as:

$$V(t) = A_D\left|R(L, j\omega)\right|\left|H(j\omega)\right| \times \sin(\omega t + \angle R(L, j\omega) + \angle H(j\omega)). \tag{31}$$

2.2.2. Parameter identification

The parameters of the IPMC sensor model needed to be identified by means of fundamental experiments. The experiment setup used to identify the IPMC model is shown in figure 8. The IPMC strip was clamped at one end. The tip of the IPMC oscillated along with a crank-slider mechanism. The apparatus could provide a periodic excitation that varied from 0.01 to 2 Hz and 2.5 to 15 mm. The clamp at the end of the slider constrained the tip of the cantilevered IPMC strip. The tip-bending deformation of the IPMC beam was correlated with the slider motion. Since the oscillation amplitude was small, the tip of the IPMC could be considered to be fixed to the slider. During the experiments, the oscillation amplitude D_a was between 5 and 15 mm. The IPMC sensor was tested under a mechanical stimulus.

The oscillation amplitude varied from 5 to 10 mm, and the frequency varied from 0.4 to 1.6 Hz. The oscillation of the IPMC strip was measured by a laser sensor (OADM 20U2441/S14C, Baumer Inc., Switzerland), and a data recorder recorded the experimental data regarding the sensing response of the sensor. Some parameters—except physical parameters

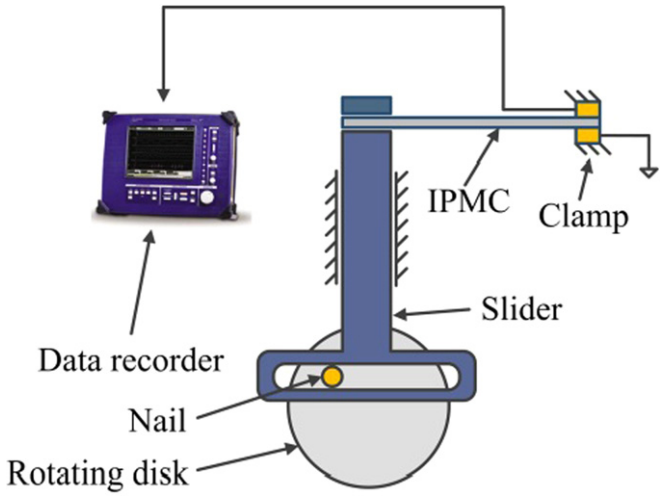

Figure 8. Schematic of the experimental set up.

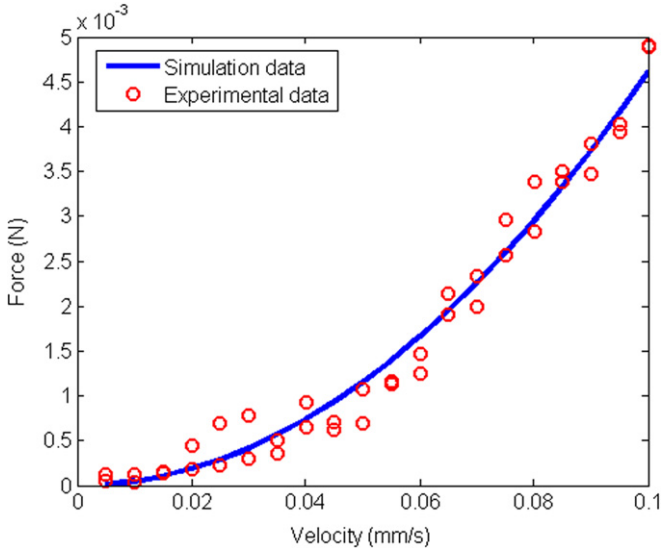

Figure 9. Drag force versus velocity of the vehicle.

(e.g., R and F) and measured directly parameters (e.g., T_a, h, and Y)—needed to be identified by means of curve fitting, using the least squares method [48].

Table 1. Parameters of the drag experiment.

Item	Value
S (m^2)	0.0179
C_D	0.0515
ρ_w (kg m^{-3})	1000

3. Results and discussion

3.1. Underwater vehicle

3.1.1. Drag coefficient

The drag force versus the towing velocity of the vehicle is shown in figure 9. Based on the experimental results, the drag coefficient, C_D, was derived. Table 1 shows the parameters of the drag experiment.

3.1.2. Speed results

The theoretical model, see (19), was verified under various operating frequencies. Figure 10 presents results of the simulation run, which had a wave frequency of 1 Hz and an amplitude of 10 mm. This figure shows the velocity of the vehicle in water in the forward direction over 20 s. Initially, the vehicle had a few fluctuating movements, and then reached steady state.

Figure 11 compares the simulation to the experimental results of the underwater vehicle speed. The predicted speeds matched the experimental data well. As the wave frequency increased, the speed of the underwater vehicle increased rapidly. The peak speed was 1.08×10^{-1} m s^{-1} at 1.6 Hz.

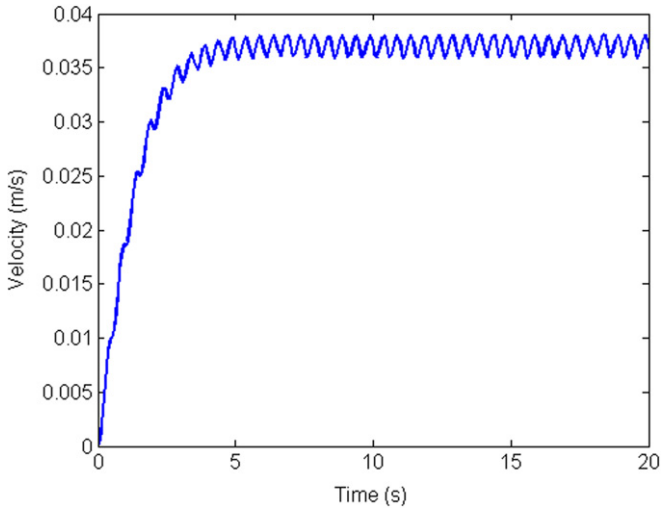

Figure 10. Simulation results for the underwater vehicle at the wave frequency of 1 Hz.

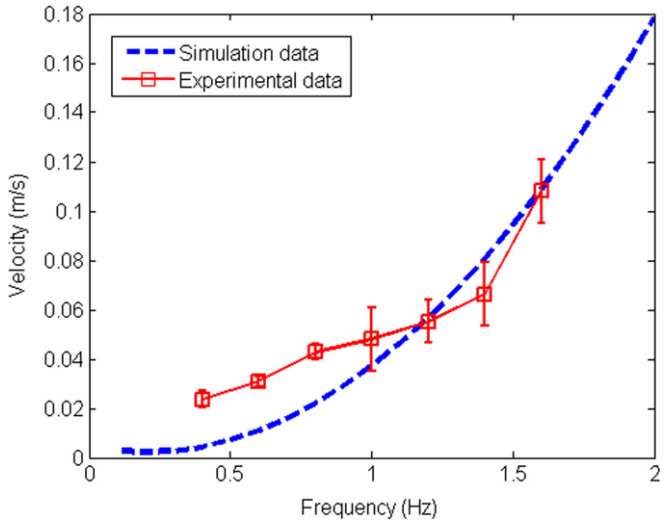

Figure 11. Simulation and experimental results of the underwater vehicle's velocities.

This study provided a prototype of the biomimetic underwater vehicle actuated by waves. The prototype can be developed further into a platform that can be applied in fields of science, commerce, and military. Apart from producing the thrust, more equipment can be applied on the submerged glider, for example, the water monitor. In addition, devices such as solar panels can be established on the float on the surface of the water. Other onboard devices—such as batteries, the control electronics, communications systems, and a variety of sensor payloads—can be replenished by the solar panels [28]. Further, a rudder can be attached to the vehicle to control the forward direction.

The Wave Glider [28] obtained an average forward speed of 1.5 kts (approximately 0.77 m s^{-1}). The ocean wave height ranged from 0.5 to 1 m. The length of the wave glider's float and glider were 2.08 and 1.91 m, respectively, and its 12 wings were 1.07 m wide. In this study, a peak speed of 1.08×10^{-1} m s^{-1} of the proposed vehicle was recorded at a wave height of 0.01 m. The float and the glider were 0.089 and 0.104 m long, respectively, and the four fins each were 0.03 m wide. Compared to systems developed in earlier studies, if the systems and the wave environment were equalized, the prototype used in this study may have had a better swimming performance. Possibly, this is because a part of the energy was consumed in the rotation of the rigid fin due to the friction inside the axles of the Wave Glider. The vehicle developed in this study utilized soft fins, and did not consume friction energy during the flapping motion, which is more efficient than other methods. However, further experiments are needed to test the vehicle in real-world applications.

Table 2. Dimensions of the IPMC strips.

Item	Length (mm)	Width (mm)	Thickness (mm)
IPMC 1	51.89	8.40	0.28
IPMC 2	38.54	8.96	0.28

Table 3. Parameters for IPMC sensor model.

Item	Value
D (m^2 s^{-1})	2.4×10^{-16}
C_0 (mol m^{-3})	154
$\hat{\varepsilon}$ (F m^{-1})	3.4×10^{-6}
μ (mol s kg^{-1})	1.8×10^{-15}
α (J C^{-1})	204

3.2. IPMC underwater sensors

3.2.1. Parameters of the model

Two IPMC samples (Environmental Robots Inc., US) of different thicknesses and sizes were tested. Table 2 shows the dimensions of IPMC samples. The experimental results were analyzed in MATLAB® (http://mathworks.com/). The parameters were derived, as shown in table 3. Figure 12 compares IPMC sensing responses with model predictions for the two IPMC strips, IPMC 1 (figure 12(a)) and IPMC 2 (figure 12(b)). Generally, the magnitude and phase of the IPMC model showed a nonlinear decrease as the frequency increased. The simulation results of the model with the identified parameters match well with the experiment results.

3.2.2. IPMC Sensors

In order to measure the output voltage of the IPMCs, the IPMC beams were attached to the soft fins and oscillated along with the fins. The frequencies of the waves varied from 0.4 to 1.6 Hz. The wave amplitude was 10 mm. The voltage of the IPMC sensors was measured by LabVIEW software (National Instruments, US).

Based on (31), the IPMC output voltage was simulated. The results for the model and experimental tests of IPMC sensors for the output voltage under various conditions matched well, as shown in figure 13. A

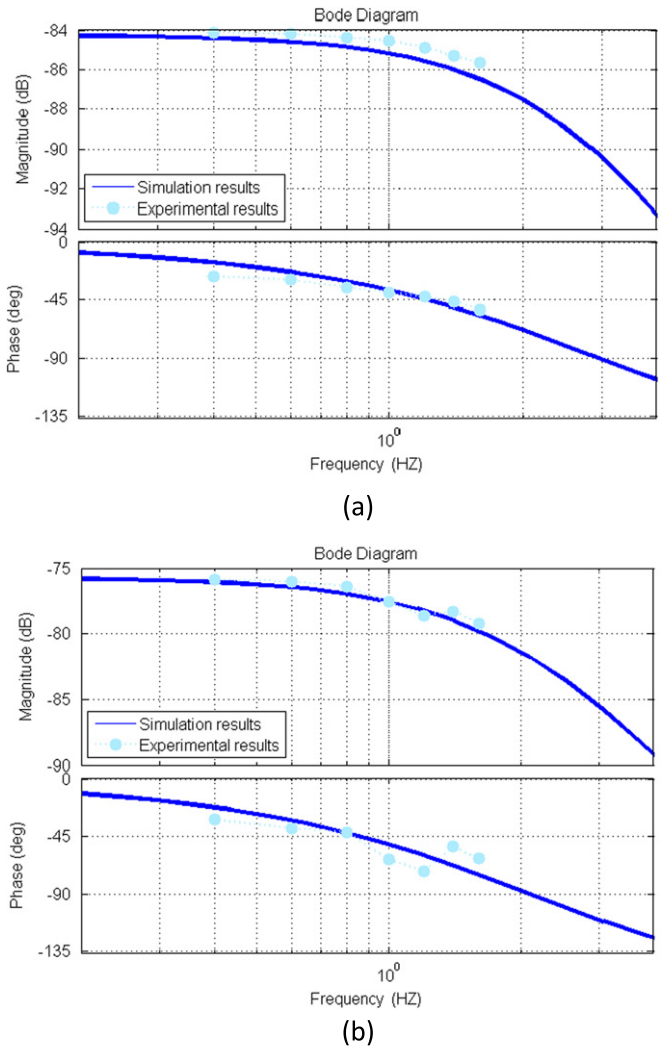

Figure 12. Comparison of the IPMC sensing response with sensing model predictions; (a) IPMC 1 having a vibration amplitude of 5 mm and (b) IPMC 2 having a vibration amplitude of 5 mm.

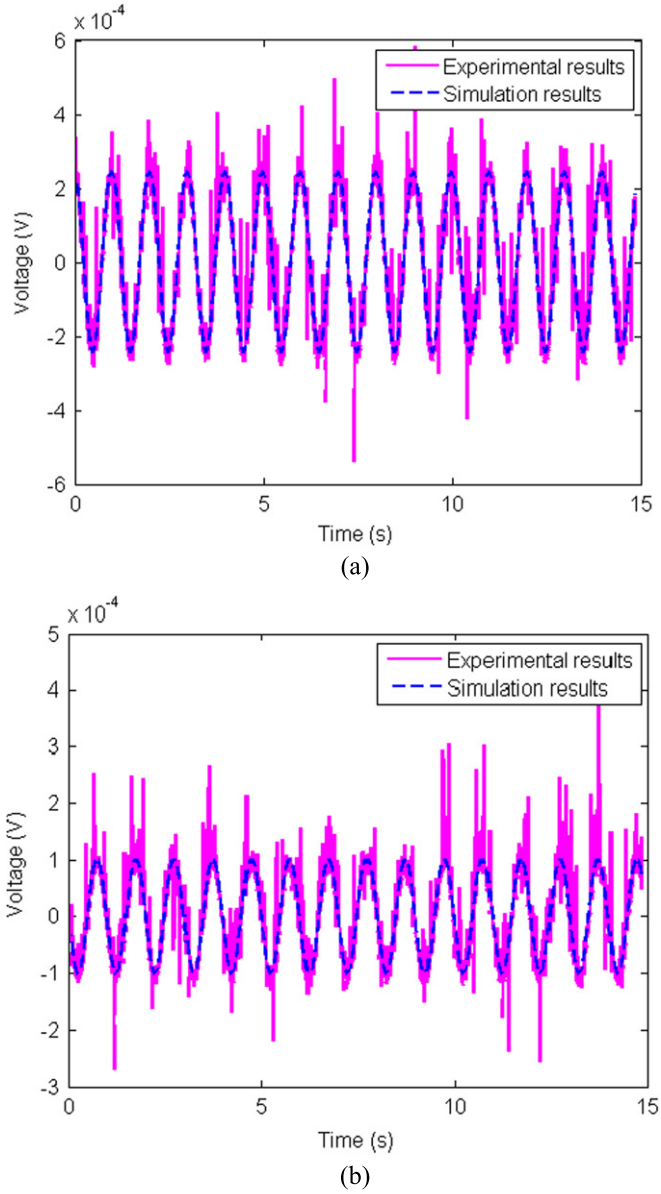

Figure 13. Simulation and experimental results of the IPMC output voltage: (a) IPMC 1 at a frequency of 1 Hz and (b) IPMC 2 at a frequency of 1 Hz.

sinusoidal voltage was tested due to the sinusoidal oscillation of the IPMC in the water.

Figure 14 shows the simulation results and experimental results of the output voltage. In generally, the output voltage of the IPMC sensors can be forecasted by the model. The amplitude of the IPMC sensor decreased with increasing wave frequency. During the steady swimming status of the underwater vehicle, the IPMCs had a stable deflection due to the stabilized wave amplitude. Based on figure 12, the magnitude of the IPMC sensor decreased as the frequency increased. Thus, the IPMC amplitude decreased as the frequency increased, which had good agreement, as shown in figure 14. A disparity was found in figure 14(b), where the magnitude of the experimental data at 1.6 Hz was larger than that of 0.4 Hz. The elucidations are as follows:

(1) The size of the tank is limited and the boundaries affected the waves. The propulsion of the underwater vehicle was influenced.

(2) The track of the underwater vehicle was not strictly straight line in the free swimming steady state, which also affected the voltage output of the IPMC sensor.

A maximum voltage amplitude of 2.27×10^{-4} V was recorded at 0.8 Hz. By comparing the voltage between IPMC 1 and IPMC 2, it was found that the voltage amplitude of IPMC 1 generally was higher than IPMC 2. Based on table 2, the length of IPMC 1 is 34.64% higher than that of IPMC 2 and the width of IPMC 1 is 6.25% lower than that of IPMC 2. Previous works on IPMC sensors also shown that under the

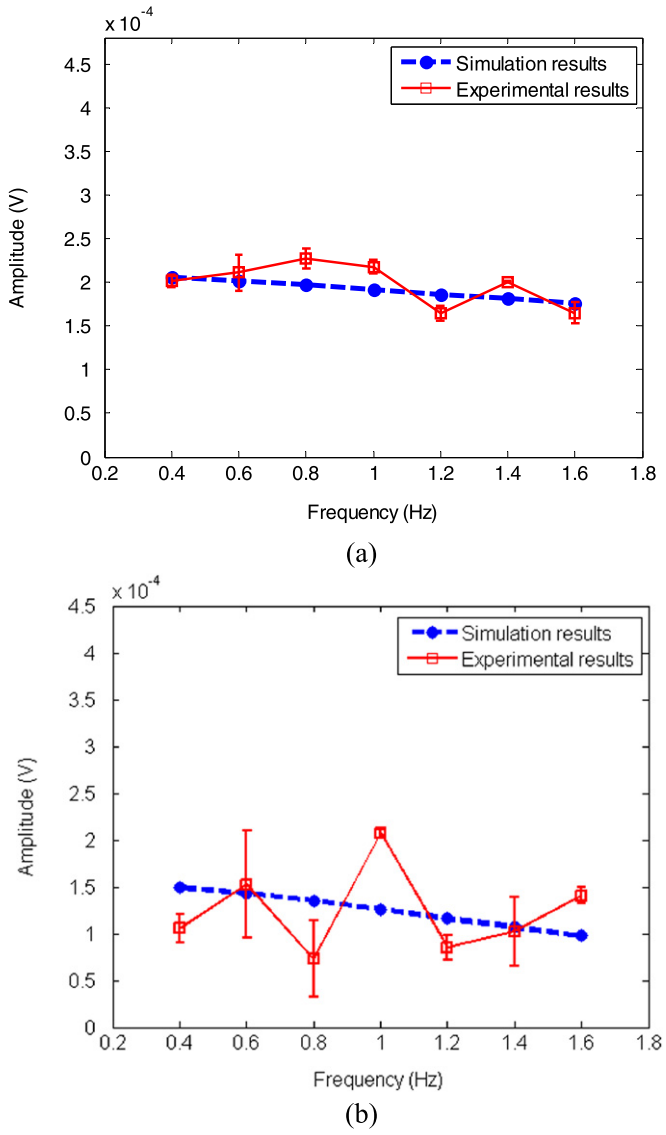

Figure 14. Simulation and experimental results of the IPMC output amplitude: (a) IPMC 1 and (b) IPMC 2.

same conditions, with the width of IPMC sensor increasing, the output of IPMC increases [35]. One may conclude that the effect of the length is dominant on the voltage output of IPMC in current system. Thus, it can be demonstrated that by increasing the length of the IPMC sensor, the voltage output will increases. Considering the results of previous work [35], it can also be indicated that the voltage output of IPMC sensor can be increased by increasing the width.

IPMCs potentially could be applied in swimming structures, biomimetic robotics, and underwater systems [49–51]. Over the past few years, significant interest has developed in using IPMC materials for underwater actuation, sensing, and energy harvesting. In this study, IPMC materials were chosen for the sensors applied on the underwater vehicle for several reasons. First, the IPMCs are appropriate for working in liquid, and they have direct mechano-sensory properties. These characteristics made it relatively easy to construct the sensor and its readout circuitry. Second, IPMC sensors have the advantage of inherent softness. This property allows the sensors to sway along with the fins of the underwater vehicle. Finally, the IPMCs are relatively simple to fabricate. Over the past decade, extensive work has been done to improve the fabrication processes. In particular, well-known processes could be used to fabricate IPMC strips on the scale of millimeters and above [52], and then cut them into any desired size.

In addition, the fins could be replaced by an IPMC sheet having the necessary material mechanical properties. The experimental results of the IPMC sensors show that the soft fins of the underwater vehicle have a sinusoid oscillation, which was in accordance with the model's predictions. By rearranging (31), a physical model of the wave could be obtained by IPMC sensors. Moreover, the wave amplitude and frequency can be measured in real time over a broad frequency range. However, the ability of the IPMC sensors in seawater remains to be validated.

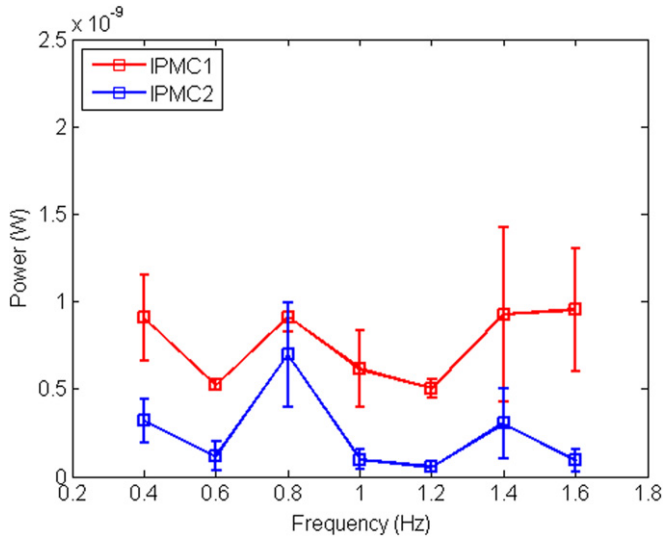

Figure 15. Experimental results of the harvested power of the IPMCs.

3.2.3. Energy harvesting capabilities of IPMC

The development of modern wireless technology requires alternative energy sources to replace traditional batteries. Such equipment as large wireless sensor networks require reliable and enduring power sources [53]. Low-power electronic devices can be powered by energy harvested from the environment [54, 55]. With their mechanoelectrical characteristics, softness, the ability to work underwater, and biocompatibility, IPMCs have promising applications in energy harvesting.

Current study investigated the energy harvesting capabilities of the underwater vehicle hosting the IPMCs. The IPMCs were connected to an external electrical load R_l of 15 Ω seperately. By measuring the voltage on the electrical load U_l, the power of the IPMC can be obtained by:

$$P_l = \frac{\int_{t_s}^{t_s+1/f} U_l^2 \, \mathrm{d}t}{R_l \cdot 1/f}. \tag{32}$$

Figure 15 shows data regarding harvested power from two types of IPMCs in the underwater vehicle. Generally, the power of IPMC 1 was greater than that of IPMC 2. The result of figure 15 is in agreement with that of figure 14. Combing with above discussion of the effect of length and width on the voltage output of IPMC, one may conclude that by increasing the length of the IPMC and the width, the power of the IPMC can be increased. The harvested power lies in the range 10^{-11} to 10^{-9} W, which has good agreement with other studies of IPMC energy harvesting [39]. A maximum power of 9.5×10^{-10} W was recorded at 1.6 Hz.

4. Conclusion

Plenty of underwater vehicles have been designed and applied in various fields. As far as we know, quite a few studies have been done regarding biomimetic clean-energy underwater systems and their hydrodynamics. This paper proposes a biomimetic underwater vehicle actuated by waves, and the swimming performance of the underwater vehicle was studied both theoretically and experimentally. The underwater vehicle was able to convert wave energy into propulsion energy. The vehicle can obtain limitless propulsion from the substantial power of the ocean waves.

A speed model of the underwater vehicle was developed. The model took into consideration the underlying hydrodynamic interactions between the soft fins and the fluid. The hydrodynamic force acting on a soft fin was modeled by integrating the hydrodynamic force on each segment of the soft fin. The generalized physical force on the fin, introduced by the motion of the wave glider, was decomposed into a distributed force along the length and a concentrated bending moment at the beam end. For the dynamics of a soft fin in fluid, the solution was derived to a fourth-order partial differential equation that incorporated the hydrodynamic force acting on the soft fin and the driving force introduced by motion of the wave glider. Thus, a speed model of the biomimetic underwater vehicle was achieved.

Experimental apparatuses were developed for testing purposes. The vehicle's speed was measured while it was freely swimming in a water tank. Under a servo towing system, drag experiments were performed to identify the parameters. When the experimental results were compared with the theoretical predictions under various operating frequencies, it was found that the model could

predict the cruising speed of the underwater vehicle with good accuracy. In addition, this study showed that the speed increased with increased wave frequency. Potentially, this vehicle has wide application, and could be beneficial in designing and optimizing biomimetic clean-energy underwater systems.

IPMCs were applied to the underwater vehicles as sensors. A physical model was developed to provide insights regarding the mechanism of the mechanoelectrical response of IPMC. The Poisson–Nernst–Planck system of equations was used to describe the charge redistribution dynamics in the polymer. The partial differential equation was solved by converting the basic equation from the time domain to the Laplace domain. The derived open-circuit sensing voltage was related to the mechanical deformation. By coordinating the beam dynamics of the soft fins and the physical model of the IPMC, the sensing voltage of the IPMCs on the underwater vehicle was obtained. Experiments were conducted to validate the model by measuring the sensing voltages of the IPMCs. The experimental results matched the theoretical results with good accuracy. Simulations were conducted to envision the proposed model, and hydrodynamic experiments were performed on the IPMC sensors. Based on the theoretical results and experimental results, it was found that the model can well predict the output of the IPMC sensors. With further experimental investigations, both the IPMC sensors and the model may also be useful in measuring the real-time wave amplitude and frequency. Additionally, the energy-harvesting capabilities of the IPMC in the underwater vehicle were investigated.

Further improvements will be made on this vehicle to support real-world applications. A theoretical model for the mechanism of IPMC energy harvesting will be developed, and more experiments will be conducted for a comprehensive understanding of IPMC energy harvesters. Furthermore, a vision based velocity measurement apparatus will be developed and the underwater vehicle will be tested in experiments.

Acknowledgments

This work is supported by National Natural Science Foundation of China (No. 61333016 and No. 61403012). Also, KJK thanks the partial financial support from the US National Science Foundation (No. 1265123). Many thanks go to Lei Bao and Zhongyu Wang from Beihang University for their help during the experimental investigation.

References

[1] Liang J, Wang T and Wen L 2011 Development of a two-joint robotic fish for real-world exploration *J. Field Robot.* **28** 70–9
[2] Yu J, Su Z, Wang M, Tan M and Zhang J 2012 Control of yaw and pitch maneuvers of a multilink dolphin robot *IEEE Trans. Robot.* **28** 318–29
[3] Zhou C and Low K H 2012 Design and locomotion control of a biomimetic underwater vehicle with fin propulsion *IEEE/ASME Trans. Mechatronics* **17** 25–35
[4] Wen L, Wang T, Wu G, Liang J and Wang C 2012 Novel method for the modeling and control investigation of efficient swimming for robotic fish *IEEE Trans. Ind. Electron.* **59** 3176–88
[5] Wen L, Wang T, Wu G and Liang J 2013 Quantitative thrust efficiency of a self-propulsive robotic fish: experimental method and hydrodynamic investigation *IEEE/ASME Trans. Mechatronics* **18** 1027–38
[6] Guo S, Fukuda T and Asaka K 2003 A new type of fish-like underwater microrobot *IEEE/ASME Trans. Mechatronics* **8** 136–41
[7] Kopman V and Porfiri M 2013 Design, modeling, and characterization of a miniature robotic fish for research and education in biomimetics and bioinspiration *IEEE/ASME Trans. Mechatronics* **18** 471–83
[8] Hu T, Low K H, Shen L and Xu X 2014 Effective phase tracking for bioinspired undulations of robotic fish models: a learning control approach *IEEE/ASME Trans. Mechatronics* **19** 191–200
[9] Su Z, Yu J, Tan M and Zhang J 2014 Implementing flexible and fast turning maneuvers of a multijoint robotic fish *IEEE/ASME Trans. Mechatronics* **19** 329–38
[10] Liu F, Lee K M and Yang C J 2012 Hydrodynamics of an undulating fin for a wave-like locomotion system design *IEEE/ASME Trans. Mechatronics* **17** 554–62
[11] Zhang F, Thon J, Thon C and Tan X 2014 Miniature underwater glider: design and experimental results *IEEE/ASME Trans. Mechatronics* **19** 394–9
[12] Ming A, Park S, Nagata Y and Shimojo M 2009 Development of underwater robots using piezoelectric fiber composite *Proc. IEEE Int. Conf. on Robotics and Automation (Kobe, Japan, 2009)* pp 3821–6
[13] Rossi C, Colorado J, Coral W and Barrientos A 2011 Bending continuous structures with SMAs: a novel robotic fish design *Bioinsp. Biomim.* **6** 045005
[14] Zhang Z, Philen M and Neu W 2010 A biologically inspired artificial fish using flexible matrix composite actuators: analysis and experiment *Smart Mater. Struct.* **19** 094017
[15] Pugal D, Kim K J, Punning A, Kasemägi H, Kruusmaa M and Aabloo A 2008 A self-oscillating ionic polymer–metal composite bending actuator *J. Appl. Phys.* **103** 084908-8-6
[16] Shahinpoor M and Kim K J 2001 Ionic polymer–metal composites: I. Fundamentals *Smart Mater. Struct.* **10** 819
[17] Shahinpoor M and Kim K J 2005 Ionic polymer–metal composites: IV. Industrial and medical applications *Smart Mater. Struct.* **14** 197
[18] Kim S M and Kim K J 2008 Palladium buffer-layered high performance ionic polymer–metal composites *Smart Mater. Struct.* **17** 035011
[19] Kim K J, Yim W, Paquette J W and Kim D 2007 Ionic polymer–metal composites for underwater operation *J. Intel. Mat. Syst. Str.* **18** 123–31
[20] Shen Q, Wang T, Wen L, Liang J and Chen Y 2012 On the thrust efficiency of an IPMC actuated robotic swimmer: dynamic modeling and experimental investigation *Proc. Int. Offshore and Polar Engineering Conf. (Rhodes, Greece, 2012)* pp 556–62
[21] Shen Q, Wang T, Wen L and Liang J 2013 Modelling and fuzzy control of an efficient swimming ionic polymer–metal composite actuated robot *Int. J. Adv. Robot. Syst.* **10** 350
[22] Wang T, Shen Q, Wen L and Liang J 2012 On the thrust performance of an ionic polymer–metal composite actuated robotic fish: modeling and experimental investigation *Sci. China Tech. Sci.* **55** 3359–69
[23] Shen Q, Wang T, Liang J and Wen L 2013 Hydrodynamic performance of a biomimetic robotic swimmer actuated by ionic polymer–metal composite *Smart Mater. Struct.* **22** 075035
[24] Shen Q, Wang T, Wen L, Liang J, Yang X and Yao G 2013 A novel method for investigating the kinematic effect on the hydrodynamics of robotic fish *IEEE Int. Conf. on Robotics and Biomimetics (Shenzhen, China, 2013)* pp 1306–11

[25] Chen Z, Shatara S and Tan X 2010 Modeling of biomimetic robotic fish propelled by an ionic polymer–metal composite caudal fin *IEEE/ASME Trans. Mechatronics* **15** 448–59
[26] Jones W D 2008 Update-ocean power catches a wave *IEEE Spectr.* **45** 14–14
[27] Willcox S, Meinig C, Sabine C L, Lawrence-Slavas N, Richardson T, Hine R and Manley J X 2009 An autonomous mobile platform for underway surface carbon measurements in open-ocean and coastal waters *Proc. MTS/IEEE OCEANS 2009 (Biloxi, USA, 2009)* pp 1–8
[28] Manley J and Willcox S 2010 The wave glider: a persistent platform for ocean science *Proc. OCEANS 2010 IEEE-Sydney (Sydney, Australia, 2010)* pp 1–5
[29] Mojarrad M and Shahinpoor M 1997 Ion-exchange-metal composite sensor films *Proc. SPIE in Smart Structures and Materials (San Diego, USA, 1997)* pp 52–60
[30] Keshavarzi A, Shahinpoor M, Kim K J and Lantz J W 1999 Blood pressure, pulse rate, and rhythm measurement using ionic polymer–metal composite sensors *Proc. SPIE in Smart Structures and Materials (Newport Beach, USA, 1999)* pp 369–76
[31] Pugal D, Jung K, Aabloo A and Kim K J 2010 Ionic polymer–metal composite mechanoelectrical transduction: review and perspectives *Polym. Int.* **59** 279–89
[32] Kim K J, Shahinpoor M and Razani A 1999 Preparation of IPMCs for use in fuel cells, electrolysis, and hydrogen sensors *Proc. SPIE in Smart Structures and Materials (Newport Beach, USA, 1999)* pp 311–20
[33] Shahinpoor M, Bar-Cohen Y, Simpson J O and Smith J 1998 Ionic polymer–metal composites (IPMCs) as biomimetic sensors, actuators and artificial muscles—a review *Smart Mater. Struct.* **7** R15
[34] Shahinpoor M and Kim K J 2002 Novel ionic polymer–metal composites equipped with physically loaded particulate electrodes as biomimetic sensors, actuators and artificial muscles *Sensors Actuators* A **96** 125–32
[35] Chen Z, Tan X, Will A and Ziel C A dynamic model for ionic polymer–metal composite sensors *Smart Mater. Struct.* **16** 1477
[36] Abdulsadda A T and Tan X 2012 An artificial lateral line system using IPMC sensor arrays *Inter. J. Smart Nano Mater.* **3** 226–42
[37] Abdulsadda A T and Tan X 2013 Underwater tracking of a moving dipole source using an artificial lateral line: algorithm and experimental validation with ionic polymer–metal composite flow sensors *Smart Mater. Struct.* **22** 045010
[38] Aureli M, Prince C, Porfiri M and Peterson S D 2010 Energy harvesting from base excitation of ionic polymer metal composites in fluid environments *Smart Mater. Struct.* **19** 015003
[39] Giacomello A and Porfiri M 2011 Underwater energy harvesting from a heavy flag hosting ionic polymer metal composites *J. Appl. Phys.* **109** 084903
[40] Cha Y, Verotti M, Walcott H, Peterson S D and Porfiri M 2013 Energy harvesting from the tail beating of a carangiform swimmer using ionic polymer–metal composites *Bioinsp. Biomim.* **8** 036003
[41] Tiwari R and Kim K J 2013 IPMC as a mechanoelectric energy harvester: tailored properties *Smart Mater. Struct.* **22** 015017
[42] Prempraneerach P, Hover F S and Triantafyllou M S 2003 The effect of chordwise flexibility on the thrust and efficiency of a flapping foil *Proc. 13th Int. Symp. Unmanned Untethered Submersible Techn. (Durham, USA, 2003)* pp 24–7
[43] Cai Y, Bi S and Zheng L 2010 Design and experiments of a robotic fish imitating cow-nosed ray *J. Bionic. Eng.* **7** 120–6
[44] Schultz W W and Webb P W 2002 Power requirements of swimming: do new methods resolve old questions? *Integr. Comp. Biol.* **42** 1018–25
[45] Sader J E 1998 Frequency response of cantilever beams immersed in viscous fluids with applications to the atomic force microscope *J. Appl. Phys.* **84** 64–76
[46] Van Dorn W G 1974 *Oceanography and Seamanship* (New York: Dodd, Mead)
[47] Nemat-Nasser S and Li J Y 2000 Electromechanical response of ionic polymer–metal composites *J. Appl. Phys.* **87** 3321–31
[48] Chen Z and Tan X 2008 A control-oriented and physics-based model for ionic polymer–metal composite actuators *IEEE/ASME Trans. Mechatronics* **13** 519–29
[49] Takagi K, Yamamura M, Luo Z W, Onishi M, Hirano S, Asaka K and Hayakawa Y 2009 Development of a rajiform swimming robot using ionic polymer artificial muscles *Proc. IEEE Int. Conf. on Intelligent Robots and Systems (Beijing, China, 2009)* pp 1861–6
[50] Nakadoi H, Sobey D, Yamakita M and Mukai T 2008 Liquid environment-adaptive IPMC fish-like robot using extremum seeking feedback *Proc. IEEE/RSJ Int. Conf. on Intelligent Robots and Systems (Nice, France, 2008)* pp 3089–94
[51] Najem J, Sarles S A, Akle B and Leo D J 2012 Biomimetic jellyfish-inspired underwater vehicle actuated by ionic polymer metal composite actuators *Smart Mater. Struct.* **21** 094026
[52] Kim K J and Shahinpoor M 2003 Ionic polymer–metal composites: II. Manufacturing techniques *Smart Mater. Struct.* **12** 65
[53] Raghunathan V, Schurgers C, Park S and Srivastava M B 2002 Energy-aware wireless microsensor networks *IEEE Signal Proc. Mag.* **19** 40–50
[54] Mitcheson P D, Yeatman E M, Rao G K, Holmes A S and Green T C 2008 Energy harvesting from human and machine motion for wireless electronic devices *Proc. IEEE* **96** 1457–86
[55] Yeatman E M 2009 Energy harvesting: small scale energy production from ambient sources *Proc. SPIE in Smart Structures and Materials (San Diego, USA, 2009)* pp 728802-2-7